A Sustainable HydrogelBased DyeSensitized Solar Cell Coupled to an Integrated Supercapacitor for Direct Indoor LightEnergy Storage

A Sustainable Hydrogel-Based Dye-Sensitized Solar Cell Coupled to an Integrated Supercapacitor for Direct Indoor Light-Energy Storage

*Sara Domenici, Roberto Speranza, Federico Bella, Andrea Lamberti, and Teresa Gatti**

The rapid growth of the Internet of Things ecosystem has increased the need for sustainable, cost-effective energy sources for indoor low-power devices. Indoor photovoltaics offer a solution by harnessing ambient indoor lighting, with dye-sensitized solar cells (DSSCs) emerging as strong candidates for these applications. When it comes to indoor environments, there is an increased demand for nontoxic and nonflammable solvents for electrolytes. The use of water-based electrolytes is a promising way to address these issues, while ensuring the eco-friendliness and sustainability of these devices. Herein, a DSSC system is employed featuring an aqueous gel electrolyte composed of xanthan gum, a biosourced polymer, and an iodide/triiodide redox couple. The performances of the cells are characterized under LED lighting, reaching efficiencies up to 3.5% in indoor conditions, and then integrated with an electric double-layer capacitor, also based on a xanthan gum gel electrolyte, resulting in a fully aqueous device for indoor light-energy harvesting and storage with an overall photoelectric conversion and storage efficiency of 1.45%.

1. Introduction

As the Internet of Things (IoT) ecosystem has rapidly expanded in recent years, vast networks of interconnected low-power devices are set to gather extensive data from their surroundings, playing a crucial role in enhancing our quality of life and the efficiency of our industries. Over the coming decade, billions of wireless sensors are expected to be installed, with a substantial amount located inside buildings.[1,2] This has created a critical need for energy sources for such devices that are both sustainable and cost-effective.[3] Indeed, traditional IoT devices are powered by batteries, which introduce several challenges related to both sustainability and scalability.[4,5] A solution for this issue is represented by indoor photovoltaics (IPV), which harness light from artificial indoor sources to generate power for IoT devices, reducing the need for frequent battery replacements and promoting energy efficiency in smart environments.[2,6,7]

Recently, thin-film third-generation PV technologies, including perovskite solar cells,[8–13] organic PV,[5,14–16] and dye-sensitized solar cells (DSSCs),[7,17–20] have been investigated for use in indoor environments. These technologies have proven to be highly versatile because it is possible to tune the bandgap through chemical modification of materials,[21] allowing them to be tailored to match the emission spectra of artificial lighting. Moreover, indoor conditions are milder (absence of UV radiation, moderate temperatures, controlled humidity) compared to outdoor solar conditions, where these technologies typically exhibit lower stability.[22,23] As a result, achieving good stability is less challenging indoors.

So far, among all PV technologies tested for specific indoor use, DSSCs have demonstrated significant potential due to several key benefits.[24–26] They show good performance in diffuse and low-light conditions[18] and offer a tunable photoresponse by selecting different sensitizers,[7] allowing their absorption characteristics to be adjusted to match specific light sources. Furthermore, DSSCs are recognized for their lower production costs and easy fabrication compared to other photovoltaic technologies,[27] making them an economically attractive option for large-scale deployment in indoor settings.[28–30] These factors, combined together, position DSSCs as promising candidates for sustainable energy harvesting for powering indoor devices. To truly offer a sustainable solution for powering IoT devices, it is also crucial to address not only the economic viability, but also the environmental impact of IPV. This means minimizing negative impacts on the environment by ensuring that materials used are nonhazardous and free from toxic components and that processing methods with low toxicity and minimal environmental impact are selected.[1,2,31,32] In this regard, it is important

S. Domenici, R. Speranza, F. Bella, A. Lamberti, T. Gatti
Department of Applied Science and Technology
Politecnico di Torino
C.so Duca degli Abruzzi 24, 10129 Torino, Italy
E-mail: teresa.gatti@polito.it

S. Domenici, R. Speranza, F. Bella, A. Lamberti
Center for Sustainable Future Technologies
Istituto Italiano di Tecnologia
Via Livorno 60, 10144 Torino, Italy

T. Gatti
Center for Materials Research
Justus-Liebig University
Heinrich-Buff-Ring 16-17, 35392 Giessen, Germany

The ORCID identification number(s) for the author(s) of this article can be found under https://doi.org/10.1002/solr.202400838.

DOI: 10.1002/solr.202400838

to note that conventional high-efficiency DSSC systems typically use organic solvent-based electrolytes, such as acetonitrile and 3-methoxypropionitrile. These solvents are characterized by high vapor pressure and volatility, which can lead to electrolyte leakage and decreased photovoltaic performance over time, and pose toxicity and flammability risks, raising safety concerns during fabrication and operation.[33–35] This has prompted researchers to explore water as a solvent medium,[20,34–38] which minimizes costs and also significantly reduces the aforementioned concerns. Furthermore, creating solid or quasisolid polymer electrolytes by trapping the liquid electrolyte in polymeric matrices is an attractive option for further enhancing long-term cell stability.[39] However, many common polymers employed for this purpose, such as polyethylene glycol, polyvinyl alcohol, and polyacrylonitrile, are derived from nonrenewable petroleum sources.[34,40,41] Therefore, additional efforts have been made to substitute these options with more sustainable alternatives, including the use of bio-based and waste-derived polymers.[40,42] Some examples of bio-based polymers that can be employed in aqueous DSSCs are lignin,[43] cellulose derivatives,[34,44] and gums.[45–47]

Herein, we report an indoor DSSC system with a hydrogel electrolyte composed of xanthan gum,[47] a nontoxic, water-soluble, and cheap polysaccharide, and I^-/I_3^- as a redox couple. To the best of our knowledge, while 100% aqueous electrolyte-based DSSCs have just recently started to be investigated for applications in indoor environments,[20,36] no evidence has been yet reported on the use of hydrogel electrolytes in such conditions. Moreover, it is crucial to take into consideration one of the major limitations regarding the use of PV cells in indoor environments, which is its dependence on an energy storage unit to overcome the intrinsic fluctuation and intermittence of light sources.[48] Solar cells have an inherently variable output which may not always match the fixed charging requirements of a battery. For instance, a solar cell's voltage might fluctuate outside the voltage range needed for efficient charging, or the current may exceed the battery's charging capacity, potentially leading to inefficiency or even damage. Additionally, batteries typically require controlled charging processes to maximize their lifespan, while solar cells' output may be irregular, especially in nonstandard applications such as indoor environments. This mismatch often requires complex power management circuits, which can increase system complexity, cost, and energy losses. On the other hand, aligning the voltage and current output of a solar cell with the optimal charging conditions for a battery continues to be a significant challenge. To avoid such limitations, a promising solution is integrating solar cells with supercapacitors.[49] Supercapacitors offer several advantages over batteries in terms of resilience to highly fluctuating input power. Unlike batteries, supercapacitors can withstand much higher intervals of charge and discharge currents, making them ideal for smoothing out the intermittent power supply from solar cells. This means that even in unpredictable indoor environments, the supercapacitor can store excess energy during periods of high illumination and release it when in the absence of light, providing a reliable energy buffer. Additionally, supercapacitors have a significantly longer cycle life compared to traditional batteries. They can endure millions of charge–discharge cycles without substantial performance degradation, which is beneficial for low-power IoT applications that require long-term reliability. Batteries, on the other hand, typically degrade over time, especially with frequent charging and discharging cycles in environments with fluctuating energy availability. Aiming to exploit these properties, a strong effort has been made to investigate the direct integration of solar cells and supercapacitor without needing additional power management circuits, providing reliable harvesting and storage systems (H&S) that could reduce system complexity, footprint, and costs.[48,50–52] Based on our current understanding, all-aqueous H&S systems have not been reported to date. Hence, in this work, we introduce a proof-of-concept all-aqueous H&S unit, which combines the previously described DSSC system with an electric double-layer capacitor (EDLC) also employing a xanthan gum-based hydrogel electrolyte.

2. Results and Discussion

The aim of this work is to implement a water-based DSSC into a working and fully water-based H&S system suitable for applications in indoor IoT devices. This is achieved by integrating the cell with an EDLC, both of them employing aqueous bio-based gel electrolytes made with xanthan gum (XG). The gel electrolyte formulation used in this work is chosen from a previous study by our group, in which a comprehensive investigation of the XG hydrogel electrolyte composition and concentrations was carried out.[47] The device architecture and methodologies employed to address the H&S system are closely aligned with those outlined in a further prior study by some of us employing an organic electrolyte.[52] Here, the aqueous devices were assembled using fluorine-doped tin oxide (FTO) conductive glass as current collector. The H&S units were first characterized separately and then an integrated device was assembled.

The XG-based solar cell (from here on referred to as XG-DSSC) was assembled using I^-/I_3^- as redox couple and D149 as sensitizer (chemical structure shown in Figure S1, Supporting Information). Previous studies have demonstrated that this dye is highly compatible with aqueous electrolytes and remains stably anchored to the photoanode when immersed in water.[37] The device was first characterized under AM 1.5G conditions (**Figure 1**a). The main PV parameters of the best-performing solar cell are reported in Table S1 (Supporting Information). The values of the main parameters obtained under solar conditions are coherent with those already reported in the literature for similar aqueous systems, also investigated in previous works by our group.[37,47,53] Compared to the XG system developed in ref. [47], where the D131 dye was used, all the main PV figures of merit values are slightly lower. This can be attributed to a poorer regeneration efficiency of the D149 dye compared to the D131 counterpart when using the I^-/I_3^- redox couple, due to a lower driving force for the reduction of the oxidized dye.[37,54] However, the high concentration of the iodine salt here used in the electrolyte helps mitigate this issue to some extent. Indeed, as observed by Law et al.[53] increasing the iodine concentration in D149 aqueous DSSCs leads to a rise in short-circuit current density (J_{SC}). Although the open-circuit voltage (V_{OC}) and fill factor (FF) experience slight reductions, a notable improvement in overall efficiency (η) is obtained. To investigate the performance of the DSSC in an indoor environment, the cell was characterized using a commercial warm white LED

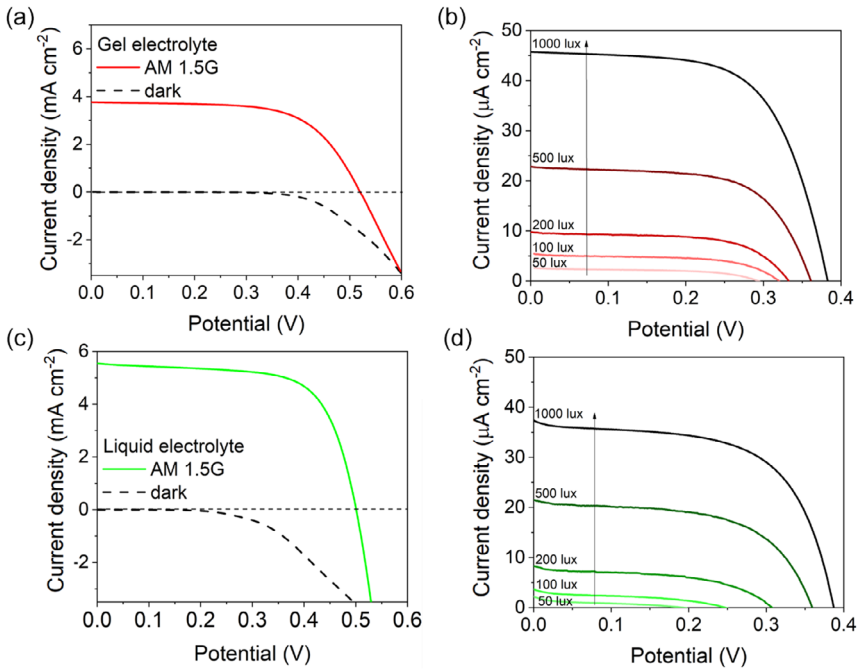

Figure 1. *J–V* curves of best performing a) XG-DSSC and c) AQ-DSSC under AM1.5G illumination and dark conditions, respectively; curves for b) XG-DSSC and d) AQ-DSSC under indoor illumination conditions at different intensities, ranging from 1000 to 50 lux.

lamp (spectral distribution shown in Figure S1, Supporting Information). As depicted in Figure S1 (Supporting Information), the D149 dye chosen for the solar cell allows for the sensitized photoanode to have an absorption spectrum which appropriately aligns with the emission spectrum of the warm white LED. The *J–V* curves were recorded at different illuminances ranging between 1000 and 50 lux (Figure 1b). These conditions are comparable to realistic indoor settings,[55] for instance the upper limit can be found in heavily lit environments, such as supermarkets, while for domestic environments the illuminance oscillates around 200 lux.[56]

Expectedly, both the V_{OC} and J_{SC} reach lower values under weaker illumination, simply due to the lower incident power. On the other hand, the lower photogeneration of electrons may also result in a lower electron-hole recombination rate, potentially leading to a higher percentage of photogenerated electrons being extracted from the photoanode.[57] More importantly, the effective spectral matching of the dye with indoor light sources, which mainly emit in the visible range, enables a better exploitation of the incident power that reaches the solar cell. In contrast, the infrared portion in the AM1.5G spectrum only contributes to energy loss without generating useful electron-hole pairs. Hence, the absence of IR radiation in indoor lighting reduces inefficiency.[58] Indeed, under low-light conditions, the DSSC exhibits significantly improved performance compared to solar illumination, achieving nearly double the efficiency at 50 lux and nearly triple the efficiency at 1000 lux. As a comparison, a liquid cell (from here on referred to as AQ-DSSC) with the same electrolyte composition, but without XG, was fabricated and characterized. Its main photovoltaic parameters, together with the respective illumination conditions, are reported in Table S1 (Supporting Information) and the respective *J–V* curves are reported in Figure 1c. Under AM1.5G conditions, the XG-DSSC shows lower J_{SC} with respect to the AQ-DSSC, which could be related both to the higher absorbance of the XG-based electrolyte compared to the liquid one, which to some extent decreases the amount of radiation reaching the photoanode, and also to reasonably slower ionic diffusion of the redox mediator within the gel electrolyte, which could limit the current flowing through the cell.[47] Indeed, the AQ-DSSC shows a better FF with respect to the XG-DSSC, which could also be related to the higher conductivity of the liquid electrolyte with respect to its gel alternative. However, while the liquid electrolyte cell shows a relatively higher efficiency under solar conditions compared to the gel electrolyte cell,[47] the same is not true under lower illumination conditions (Figure 1d).

Figure 2 shows the comparison of the main PV parameters of the two cell configurations at different indoor irradiances (P_{in}). The J_{SC} of both cells exhibits a similar trend, nearly matching current values, and a linear decrease as irradiance diminishes. Notably, the AQ-DSSC initially generates a significantly higher current under AM1.5G conditions, but eventually converges to values closely matching those of the XG-DSSC. On the other hand, the V_{OC} and FF of the AQ-DSSC drop by ≈50% and 63%, respectively, when the illumination decreases from 1000 to 50 lux. For the XG-DSSC, this reduction is limited to 24% for the V_{OC} and only 14% for the FF. Overall, the XG-DSSC efficiency remains much more consistent across the entire irradiance range. It is clear from Figure 1c that the liquid electrolyte cell is affected by a much more significant dark current compared to the hydrogel electrolyte cell. This indicates a higher rate of interfacial recombination reactions when using the liquid electrolytes with high concentrations, which likely outweigh density of photogenerated electrons.[59] A possible explanation for lower

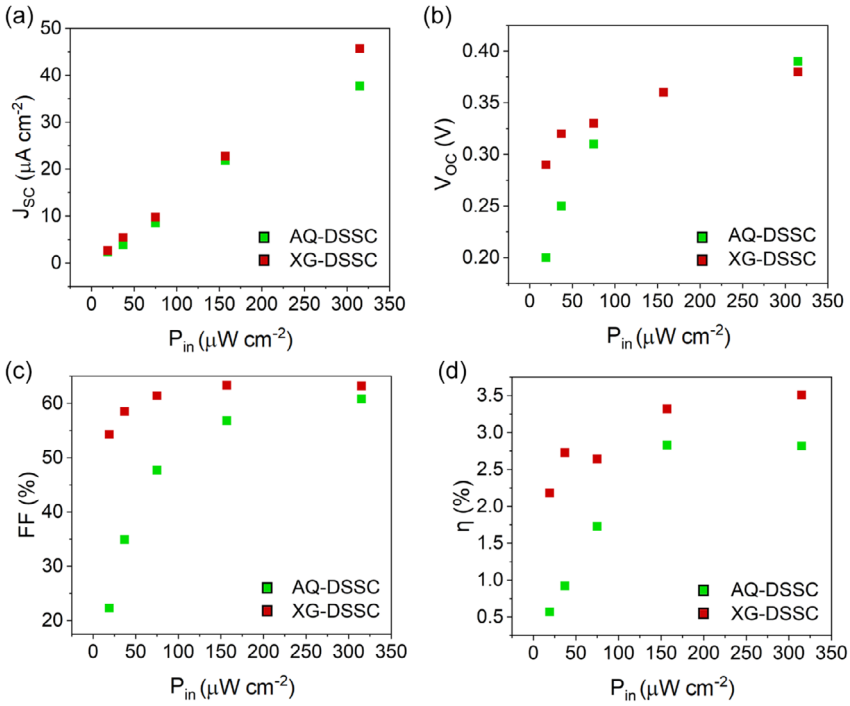

Figure 2. Main PV parameters of XG-DDSC (red dots) and AQ-DSSC (green dots) at different irradiances: a) J_{SC}, b) V_{OC}, c) FF, and d) η.

recombination processes in the hydrogel electrolyte may be due to a stabilizing effect given by XG on the redox species. Indeed, triiodide forms a supramolecular coordination complex with starch-based biopolymers,[60] which may reduce the rate of electron recombination processes simply by sterically hindering the interactions between the triiodide oxidized species itself and the sites where electrons are photogenerated. When the conversion of I_3^- to $3I^-$ at the photoanode interface is hindered, the FF[61] and V_{OC}[54] are enhanced, which may be a possible explanation for the lower parameter drops in XG-DSSC at low illumination. Overall, this initial evaluation indicates the XG-DSSC is a promising sustainable candidate in integrated indoor H&S devices.

As a suitable storage unit to be coupled with the XG-DSSC, a symmetric EDLC was fabricated on FTO glass, with the aim of constructing an integrated device in which a current collector is shared between the two units. Commercial activated carbons (AC) were employed as electrodes, particularly YP-50F, a commonly used electrode material in commercial carbon-based supercapacitors with a reported BET surface area of 1666 m^2 g^{-1}.[62–64]

The characterization of the EDLC parameters is reported in areal current density for easier system design, since the area of the active materials for the two units was kept the same. Cyclic voltammetry (CV) was performed at 10 mV s^{-1} to obtain information about its potential window and assess whether this is compatible with the V_{OC} potential range of the XG-DSSC under indoor illumination. It is clear from **Figure 3**a that no redox peaks are present in the voltammograms up to 0.5 V, far over the V_{OC} measured at the highest indoor irradiance tested. The curves maintain a rectangular shape typical of EDLCs within that potential range and maintain a high Coulombic efficiency over 90%. A slight resistive component was also observed, which has been investigated by electrochemical impedance spectroscopy (EIS), as reported in Figure S2a (Supporting Information). As shown in the inset, from the Nyquist plot it is clear how a relatively high equivalent series resistance (ESR) of 10 Ω is reasonably coming from the FTO current collector.[52] Moreover, the semicircle at higher frequencies might be related to a nonoptimal interface between the active material and the current collector.[65] Then, a vertical linear behavior at lower frequencies represents the purely capacitive contribution in the EDLC. The specific capacitance of the EDLC was calculated from the CV scan up to 0.4 V, and its value was ≈22 mF mg^{-1} (109 mF cm^{-2} in terms of areal capacitance). These values are comparable to those reported for other AC supercapacitors using starch-based hydrogel electrolytes.[66,67] Galvanostatic charge–discharge (GCD) curves were recorded at current ranges of similar magnitudes to the J_{SC} of the XG-DSSC under low irradiance and are shown in Figure 3b. The GCD curves show the typical triangular shape of EDLCs. At higher current densities, relatively significant iR drops are observed, of about 40 and 20 mV at 100 and 50 μA cm^{-2}, respectively, and can be ascribed to the elevated ESR of the device. The areal capacitance and specific capacitance were also calculated from these curves and are reported in Figure S2b (Supporting Information). A clear increase in areal/specific capacitance was observed with increasing current densities, up to 20 μA cm^{-2}. At 5 μA cm^{-2}, the capacitance remains constant, and at 2 μA cm^{-2} a steep drop is observed. This can be explained by measuring the leakage current of the supercapacitor. The leakage current is crucial for IoT applications in which an indoor light harvesting device is also implemented, since for sub-mW applications

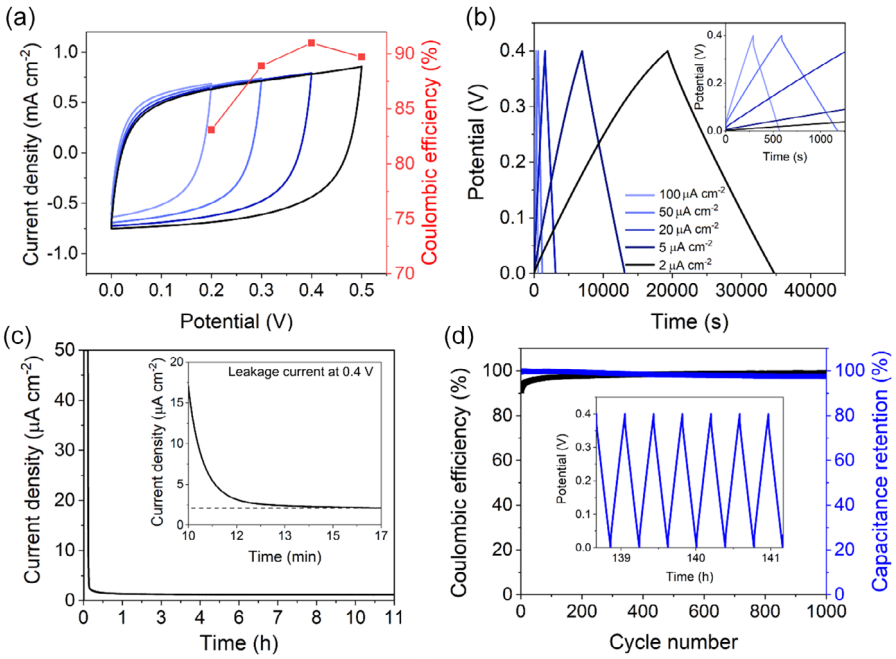

Figure 3. Characterization of an EDLC containing a starch-based hydrogel electrolyte. a) CV scans under different potential ranges performed at 10 mV s^{-1}. b) GCD voltage profiles performed at different scan rates, from 2 to 100 μA cm^{-2}, c) cycles leakage current measured when keeping the EDLC at a potential of 0.4 V over a prolonged time, and d) cycling stability test performed at 50 μA cm^{-2} over 1000 cycles.

supercapacitor internal leakage can represent a non-negligible loss impacting the overall behavior of the system.[68] As shown in Figure 3c, the leakage current profile is typical of a polymer hydrogel electrolyte supercapacitor.[69] The leakage current decreases rapidly within the first 15 min. This type of trend is particularly suitable when designing an integrated H&S device, since the leakage current has the heaviest effects on the energy loss for only a few minutes after the light is turned off. The leakage current then stabilizes at a value of around 2 μA cm^{-2}. This result is in accordance with the specific capacitance drop at 2 μA cm^{-2}, at which the leakage current begins to approach the charging current. Hence, provided that the charging current is not too close to the leakage current, these results highlight how the exploitable capacitance of the device strongly increases when it is charged at lower current rates. The suitable current ranges are comparable with the current values generated by the XG-DSSC at the selected indoor illumination conditions, down to illuminance levels of 200 lux. This suggests that the EDLC demonstrates good compatibility with the XG-DSSC harvesting unit and good potential for its integration into an H&S device. The stability of the supercapacitor was tested with 1000 GCD cycles at 50 μA cm^{-2} (Figure 3d). The device shows a very stable Coulombic efficiency of around 99%, as well as high capacitance retention of 97.5% at the last cycle. The EDLC is therefore considered suitable to be integrated with the XG-DSSC in a single H&S device, as it operates effectively within the same voltage and current ranges and can endure frequent charge–discharge cycles, which is essential considering the envisioned behavior of such H&S elements, which are expected to work as energy sources for low-power IoT electronics, accumulating excess energy during times of light availability and providing the stored energy during times of light absence (e.g., day–night cycle in indoor environments).

After characterizing the single H&S units, an integrated system was built as shown in **Figure 4**a,b.

The indoor H&S device was characterized by performing a photocharge–discharge test at 1000 lux. Figure 4c provides a schematic representation of the working mechanism of the three-electrode integrated device under illumination. In this design, the device units share a common counter electrode, while the other two electrodes remain electrically connected during light exposure. Upon illumination, the dye absorbs light and generates excited electrons, which are injected into the mesoporous TiO_2, while the redox couple regenerates the dye, as detailed in the energy diagram and excitation mechanism shown in Figure 4d.[37,70] These photogenerated electrons from the DSSC then flow through the electrical connection to the negative electrode of the EDLC, initiating the photocharging process. Owing to the fundamental properties of EDLCs, which do not require a minimum potential to initiate the charging process, the EDLC will begin charging linearly with the current supplied by the DSSC. As the charging potential approaches the V_{OC}, the current coming from the DSSC gradually decreases to zero, leading the system to reach a stationary state (plateau).

The *J*–*V* curve of the DSSC employed in the integrated device was also recorded to better understand the various contributions in the final device (Figure S3a,b, Supporting Information). The results obtained for the integrated system are shown in **Figure 5**a. The photocharging step was carried out for roughly 20 min. It was possible to charge the supercapacitor slightly over 0.4 V, because of the relatively higher V_{OC} of the cell obtained in

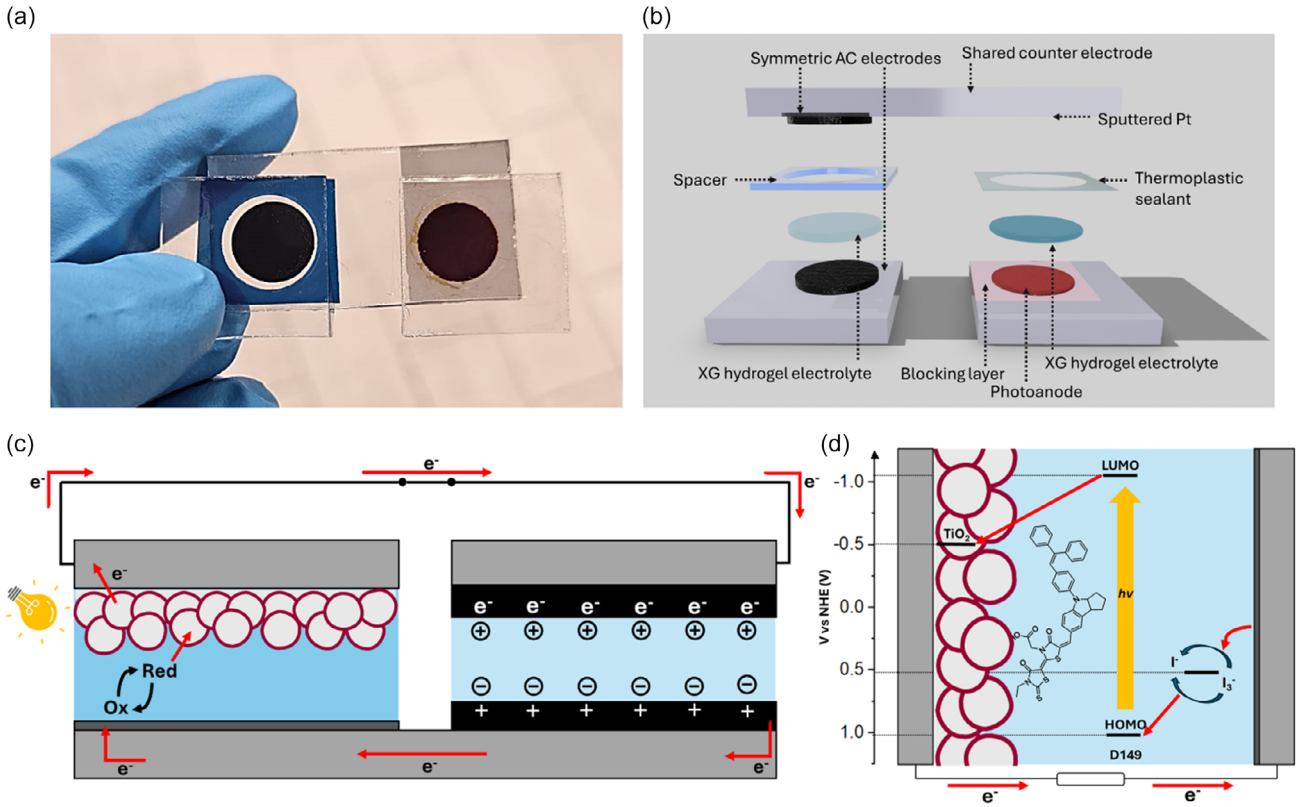

Figure 4. a) Image of the integrated H&S device containing the XG-DSSC and the XG-based EDLC and b) schematic 3D illustration showing its different layers. c) Device structure showing photocharging mechanism and d) working principle with simplified energy level diagram of the DSSC under illumination.

the resulting module. No significant plateau was observed during the photocharging process, as the very low leakage current of the supercapacitor of 2 μA cm^{-2} is fully compensated by the current generated by the solar cell up to the charging potential, of around 8 μA cm^{-2} (Figure S3b, Supporting Information). A current density of 50 μA cm^{-2} was applied to discharge the supercapacitor, and the areal capacitance calculated in this case is 80 mF cm^{-2}, comparable to that obtained in the GCD evaluation in the previous section (Figure S2b, Supporting Information).

The device's overall efficiency was assessed by calculating the overall photoelectron conversion and storage efficiency (OPECSE) as a function of both photocharging time and voltage (Figure 5c,d). In both cases, the OPECSE rises linearly, reaching up to 1.45%. When considering voltage, the OPECSE continues to increase linearly throughout the photocharging phase, peaking at a voltage that is 93% of the charging voltage, thanks to the high FF of the solar cell. When considering time, the efficiency increases linearly in the same time range in which the potential is also linearly increasing during photocharging (up to about 800 s). The slope changes as the voltage approaches the maximum voltage. After reaching its maximum value at 1030 s (roughly 17 min), the OPECSE gradually declines as the incoming electromagnetic energy remains constant while the EDLC voltage approaches maximum, hence limiting the amount of energy stored in the EDLC.[48] As a comparison, a photocharge–discharge test was performed also under solar conditions, as shown in Figure S4a,b,c (Supporting Information), using a discharge current of 100 μA cm^{-2}. This higher discharge current was selected to better align with the greater current produced by the solar cell in sunlight, reducing the gap between photocharging and discharging currents. Expectedly, the charging potential is higher, thanks to the higher V_{OC} of the solar cell (Figure S3a, Supporting Information) and the charging time is lower. The OPECSE trend with time and voltage have similar profiles as the ones observed indoor; however, the overall device performs less effectively, as the maximum obtained value of OPECSE is 0.75%. This can be ascribed to a better exploitation of the incoming power by the solar cell and the effective utilization of the capacitance of the EDLC, when charged at the low current rates provided by the solar cell.[52] Moreover, the device showed consistent photocharge–discharge performance after 45 days of storage under artificial light, with no significant changes in the profile (Figure S4d, Supporting Information), indicating minimal electrolyte leakage or material degradation. This suggests that the device holds promising performance in terms of stability during continuous operation under indoor illumination, although a more thorough investigation needs to be carried out.

The self-discharge of the device was assessed under two different conditions. First, it was measured with the two units electrically disconnected, by simply removing the connection between the negative electrodes. This was done to isolate the contribution from the EDLC leakage current alone. In the second

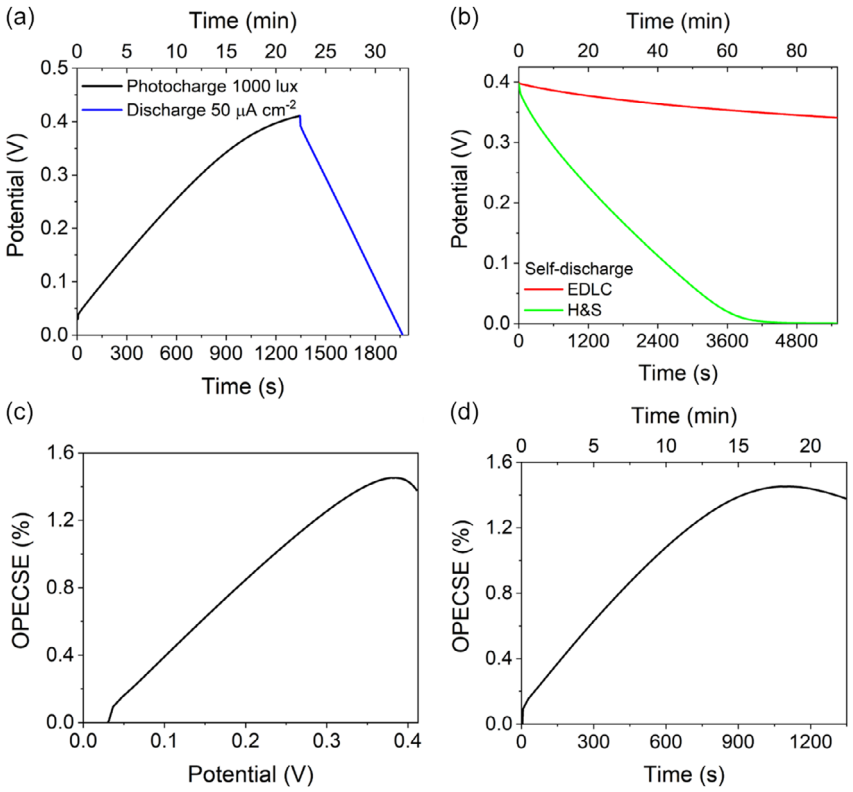

Figure 5. Characterization of the H&S hydrogel-based integrated device under indoor conditions. a) Photocharge-discharge profile performed under 1000 lux illumination and 50 μA cm^{-2} discharge constant current. b) Self-discharge profiles performed by keeping the units electrically connected (green curve) and electrically disconnecting the units (red curve). OPECSE plots as a function of c) time and d) potential.

scenario, the negative electrodes remained connected during self-discharge in the dark to assess the impact of the dark current of the solar cell on the integrated device. While the self-discharge time of the device due solely to the EDLC contribution is very long, it drops significantly to around 80 min when the units remain electrically connected. As the potential decreases, the dark current of the DSSC also diminishes, slowing down the rate of discharge further as the potential approaches lower values, as seen by the nonconstant slope of the discharge curve. Given the dark current of the XG-DSSC (Figure S3b, Supporting Information) at the maximum charging potential of ≈20 μA cm^{-2} and the fact that this dark current diminishes with decreasing potential, this discharge time is reasonable. Nonetheless, this indicates that, for the practical implementation of modules with similar systems, a blocking diode would be necessary to ensure proper device operation.[71] Although the diode causes an unavoidable voltage drop, which can hinder performance in low-voltage systems like the one presented here, increasing the module size can help alleviate this problem. Next step will be the implementation of this system in larger modules to generate the required voltage to efficiently power small IoT devices, exceeding 1 V.[72] Consequently, in a larger module, the impact of the blocking diode becomes less significant. Moreover, a comprehensive evaluation of stability and general indoor conditions will be conducted by monitoring the maximum power point during continuous operation and testing the device under other ambient light sources. Overall, these tests demonstrate that this integrated all-aqueous H&S device shows promising potential for applications in the powering of the indoor IoT ecosystem. Generally, this three-electrode integration approach is highly versatile and can be easily tailored to meet specific design requirements. A practical alternative for this system structure is a monolithic design, where the shared electrode allows the units to be stacked vertically rather than arranged in a planar configuration. This structure not only makes the device more compact but also reduces resistive losses.[73] This can be achieved by using an alternative material for the counter electrode instead of FTO, ensuring compatibility with the supercapacitor material. Both planar and monolithic configurations have also been successfully applied to perovskite and organic solar cells[74] and can also be easily implemented on other third-generation photovoltaics, such as heterojunction solar cells.[75] Further device structures and design alternatives will be explored in our future studies.

3. Conclusions

In this work, we have presented a proof-of-concept, all-aqueous indoor H&S system that employs a DSSC as an energy harvesting section and an EDLC energy storage one, both featuring sustainable, bio-based XG hydrogel electrolytes. To the best of our knowledge, this is the first reported as fully aqueous indoor H&S. We observed that the XG-DSSC demonstrates promising

potential for indoor applications, with a V_{OC} of 0.4 V and reaching efficiency of 3.5% at 1000 lux, overall showing better performance indoor compared to solar conditions. In contrast, the AQ-DSSC exhibits significantly lower performance, particularly at very low light intensities. This underscores the importance of addressing parasitic recombination mechanisms, which drastically reduce solar cell efficiency under low illumination, as recombination can give a more significant contribution compared to the photogenerated current, effects that may not be as relevant under solar conditions. We then assessed an EDLC device constructed on FTO glass with similar electrolyte matrix, with an areal capacitance of 109 mF cm^{-2} which operates effectively within the same current and potential ranges as the solar cell and shows stable Coulombic efficiency of 99% and high capacitance retention of 97.5% after 1000 cycles. This compatibility makes it well suited for successful coupling with the solar cell. After conducting these evaluations, we constructed and characterized the integrated device through photocharge–discharge tests. Under artificial illumination, this device achieves a maximum overall photoelectric conversion and storage efficiency of 1.45%, which is a promising value that suggests significant potential for further development in this field. We also observed a significant impact of the DSSC acting as a parasitic load during the device self-discharge. This indicates the necessity for a blocking diode to ensure the device operates effectively, and the development of larger modules is necessary to effectively power IoT devices.

While further optimization is needed, particularly in addressing dark current and maximizing overall efficiency, this study shows that aqueous-based DSSCs may hold considerable promise in the field of indoor light-energy harvesting and storage for IoT applications.

4. Experimental Section

Materials: Sodium iodide (NaI), iodine (I_2), XG ($M_w = 4–12 \times 10^6$ g mol^{-1}), chenodeoxycholic acid (CDCA), ethanol, acetone, t-butanol (*t*-BuOH), titanium tetrachloride ($TiCl_4$), acetonitrile (ACN), dimethyl sulfoxide (DMSO), potassium chloride (KCl), and potassium hydroxide (KOH) were purchased from Sigma–Aldrich. FTO-coated glass (15 Ω sq^{-1}), thermoplastic sealing film (60 µm, Meltonix), and Ti Nanoxide BL/SC solution were purchased from Solaronix. 5-[[4-[4-(2,2-diphenylethenyl) phenyl]-1,2,3-3a,4,8b-hexahydrocyclopent[*b*]indol-7-yl]methylene]-2-(3-ethyl-4-oxo-2-thioxo-5-thiazolidinylidene)-4-oxo-3-thiazolidineacetic acid (D149) sensitizer was purchased from Inabata Europe S.A. Transparent nanoparticle TiO_2 transparent paste (18NR-T) was purchased from Dyesol. Activated carbon (AC) YP-50 F powder was purchased from Kuraray. Carbon black (CB) C65 powder was purchased from Imerys. Polyvinylidene fluoride (PVDF) was purchased from Archema.

DSSC Fabrication: The dye solution[37] and electrolytes[47] were prepared according to an already reported procedure, here summarized. A solution of D149 dye 0.5 mM and CDCA 0.9 mM was dissolved in *t*-BuOH/ACN 1:1. The liquid and gel electrolytes were prepared using a supersaturated aqueous solution of CDCA, prepared by adding excess CDCA in water and stirring at 40 °C overnight. NaI 5 M and I_2 30 mM were added to the solution. For hydrogel electrolytes, XG 5 wt% was added and stirred for 2 h at 40 °C. FTO substrates were cut into square-shaped pieces with dimensions of 2 × 2 cm and cleaned in an ultrasonic bath with detergent, ethanol, and finally acetone. The substrates were then dried with compressed air. For the photoanode, a blocking layer of TiO_2 was deposited on a masked 1.5 × 1.5 cm area via spin coating 75 µL of Ti Nanoxide BL/SC solution at 5000 rpm for 30 s and firing at 500 °C for 1 h. The porous TiO_2 layers were deposited in circular shapes with a diameter of 10 mm (0.785 cm^2 surface area) through screen printing using a 43T mesh screen. The paste was left to dry for 10 min and was then sintered in an oven with a temperature ramp of 120 °C min^{-1}, then left at 475 °C for 45 min. A treatment was performed by submerging the TiO_2 layers in a 40 mM solution of $TiCl_4$, previously prepared using a Schlenk line, at 70 °C for 30 min and then rinsed with water, dried, and fired at 475 °C again for 1 h. The photoanodes were then heated to 70 °C and placed in the dye solution for 5 h. They were then rinsed with acetone to remove residual dye. For the liquid electrolyte cells, a hole was placed in the counter electrode to insert the electrolyte. Platinum counter electrodes were prepared by sputtering for 30 s. For liquid electrolyte devices, the cells were first sealed with thermoplastic sealing foil on a hotplate at 100 °C, and the electrolyte was injected afterward through the hole. The hole was then sealed with another piece of thermoplastic foil and a thin glass sheet. In the gel electrolyte devices, the electrolyte was spread on the photoanode with a spatula before sealing.

EDLC Fabrication: A DMSO-based slurry was prepared with a composition of AC 85 wt%, CB 5 wt%, and PVDF 10 wt% by stirring at room temperature for 24 h. FTO substrates were cut in square shaped with dimensions of 2 × 2 cm and cleaned. Masks of 1 cm diameter were prepared, and the electrodes were fabricated by depositing the slurry using doctor blade technique. The electrodes were left to dry for 4 h under a fume hood. The obtained electrodes have a thickness of 70 µm and a mass loading of 2.5 mg cm^{-2}. The electrolyte was prepared by dissolving XG 3 wt% in water. The pH of the suspension was adjusted to neutral[76] using a 5% volume of a KOH 1 M solution and checked with pH paper. KCl 2 M was added as electrolyte. The EDLC was assembled in air using double-sided tape.

H&S Device: The integrated device was prepared in a similar manner, but using a 4 × 2 cm FTO glass as shared counter electrode. First, the DSSC was sealed, followed by the assembly of the supercapacitor.

DSSC Characterizations: *J–V* curves were measured using a Keithley SourceMeter kit and a VeraSol-2 LED solar simulator (class AAA, by Oriel) under AM 1.5G illumination (100 mW cm^{-2}), calibrated with an Oriel PV reference cell system (model 91150V). The active area was delimited to 0.1256 cm^2 using a black mask. Dark current was also measured. For indoor characterizations, a low-consuming LED lamp (9 W, 2700 K, 806 lm from HUE Philips) was used. The cells were characterized inside a black box and using an Autolab potentiostat. The illuminance and incident power were measured using a Delta Ohm HD 2102.2 photo/radiometer.

EDLC Characterizations: The EDLC performance was tested with a BioLogic VMP3 potentiostat using the following techniques: CV, potentiostatic EIS (PEIS), GCD, and galvanostatic cycling with potential limitation for leakage current.

H&S Characterizations: The integrated device was characterized by performing a photocharge/constant-current discharge test under both a simulated AM1.5G spectrum and indoor LED light. The photocharge step was performed by keeping the negative electrodes of the units electrically connected, while they were disconnected during the discharge measurements. The potentiostat was connected to the electrodes of the EDLC to monitor the change in potential. Measurements were conducted using an Autolab potentiostat. During the photocharge step, the device was kept exposed to the light source as the voltage of the EDLC was measured. Following this, the EDLC was discharged at a constant current. Based on these measurements, the OPECSE was calculated

$$\mathrm{OPECSE} = \frac{\frac{1}{2} \times C \times \Delta V^2}{G \times t \times A} \quad (1)$$

where C is the capacitance of the EDLC, ΔV is the difference between the EDLC voltage and the relative open-circuit voltage, G is the incident radiation power density, t is the photocharging time, and A is the total active surface of the DSSC.

Supporting Information

Supporting Information is available from the Wiley Online Library or from the author.

Acknowledgements

S.D. and T.G. acknowledge the financial support of the European Research Council through project Nr. 101041229. This project has also received funding from the European Research Council (ERC) under the European Union's Horizon 2020 research and innovation program (grant agreement no. 948769, project title: SuN_2rise). The authors would also like to acknowledge the project "nuovi Concetti, mAteriali e tecnologie per l'iNtegrazione del fotoVoltAico negli edifici e in uno scenario di generazione diffuSa" ("CANVAS"), funded by the Italian Ministry of the Environment and Energy Security, through the Research Fund for the Italian Electrical System (type-A call, published on G.U.R.I. n.192 on 18/08/2022), the project MOST – Sustainable Mobility Center and received funding from the European Union Next-GenerationEU (PIANO NAZIONALE DI RIPRESA E RESILIENZA (PNRR) – MISSIONE 4 COMPONENTE 2, INVESTIMENTO 1.4 – D.D. 1033 17/06/2022, CN00000023) and the project CARE - CO2 Advanced, environmental-friendly nano-technology based electrochemical REduction (CARE), funded by PRIN call by MUR.

Conflict of Interest

The authors declare no conflict of interest.

Author Contributions

Sara Domenici: data curation (lead); formal analysis (lead); investigation (lead); methodology (equal); project administration (equal); writing—original draft (lead). **Roberto Speranza**: conceptualization (equal); data curation (equal); formal analysis (equal); investigation (equal); methodology (equal); supervision (equal); validation (equal); visualization (equal); writing—review and editing (equal). **Federico Bella**: conceptualization (equal); data curation (equal); funding acquisition (equal); project administration (equal); resources (equal); supervision (equal); writing—review and editing (equal). **Andrea Lamberti**: conceptualization (equal); funding acquisition (equal); project administration (equal); resources (equal); supervision (equal); writing—review and editing (equal). **Teresa Gatti**: conceptualization (equal); data curation (equal); funding acquisition (equal); project administration (equal); resources (equal); supervision (equal); validation (equal); visualization (equal); writing—review and editing (equal).

Data Availability Statement

The data that support the findings of this study are available from the corresponding author upon reasonable request.

Keywords

dye-sensitized solar cells, hydrogel electrolytes, integrated energy devices, supercapacitors, water-based devices

Received: November 26, 2024
Revised: January 16, 2025
Published online: January 29, 2025

[1] V. Pecunia, L. G. Occhipinti, R. L. Z. Hoye, *Adv. Energy Mater.* **2021**, *11*, 2100698.
[2] I. Mathews, S. N. Kantareddy, T. Buonassisi, I. M. Peters, *Joule* **2019**, *3*, 1415.
[3] H. Elahi, K. Munir, M. Eugeni, S. Atek, P. Gaudenzi, *Energies* **2020**, *13*, 5528.
[4] M. Shirvanimoghaddam, K. Shirvanimoghaddam, M. M. Abolhasani, M. Farhangi, V. Zahiri Barsari, H. Liu, M. Dohler, M. Naebe, *IEEE Access* **2019**, *7*, 94533.
[5] M. Jahandar, S. Kim, D. C. Lim, *ChemSusChem* **2021**, *14*, 3449.
[6] X. Hou, Y. Wang, H. K. H. Lee, R. Datt, N. Uslar Miano, D. Yan, M. Li, F. Zhu, B. Hou, W. C. Tsoi, Z. Li, *J. Mater. Chem. A* **2020**, *8*, 21503.
[7] H. Michaels, M. Rinderle, I. Benesperi, R. Freitag, A. Gagliardi, M. Freitag, *Chem. Sci.* **2023**, *14*, 5350.
[8] G. K. Grandhi, B. Al-Anesi, H. Pasanen, H. Ali-Löytty, K. Lahtonen, S. Granroth, N. Christian, A. Matuhina, M. Liu, A. Berdin, V. Pecunia, P. Vivo, *Small* **2022**, *18*, 2203768.
[9] R. Cheng, C. C. Chung, H. Zhang, F. Liu, W. T. Wang, Z. Zhou, S. Wang, A. B. Djurišić, S. P. Feng, *Adv. Energy Mater.* **2019**, *9*, 1901980.
[10] C. Zhang, C. Liu, Y. Gao, S. Zhu, F. Chen, B. Huang, Y. Xie, Y. Liu, M. Ma, Z. Wang, S. Wu, R. E. I. Schropp, Y. Mai, *Adv. Sci.* **2022**, *9*, 2204138.
[11] C. Teixeira, P. Spinelli, L. A. Castriotta, D. Müller, S. Öz, L. Andrade, A. Mendes, A. Di Carlo, U. Würfel, K. Wojciechowski, D. Forgács, *Adv. Funct. Mater.* **2022**, *32*, 2206761.
[12] X. He, J. Chen, X. Ren, L. Zhang, Y. Liu, J. Feng, J. Fang, K. Zhao, S. Liu, *Adv. Mater.* **2021**, *33*, 2100770.
[13] Z. Skafi, J. Xu, V. Mottaghitalab, L. Mivehi, B. Taheri, F. Jafarzadeh, S. K. Podapangi, D. Altamura, M. R. Guascito, L. Barba, C. Giannini, A. Rizzo, F. De Rossi, H. Javanbakht Lomeri, L. Sorbello, F. Matteocci, F. Brunetti, T. M. Brown, *Sol. RRL* **2023**, *7*, 2300324.
[14] Y. Cui, Y. Wang, J. Bergqvist, H. Yao, Y. Xu, B. Gao, C. Yang, S. Zhang, O. Inganäs, F. Gao, J. Hou, *Nat. Energy* **2019**, *4*, 768.
[15] T. H. Kim, N. W. Park, M. A. Saeed, S. Y. Jeong, H. Y. Woo, J. H. Park, J. W. Shim, *Nano Energy* **2023**, *112*, 108429.
[16] P. Bi, C. An, T. Zhang, Z. Chen, Y. Xu, Y. Cui, J. Wang, J. Li, Y. Wang, J. Ren, X. Hao, S. Zhang, J. Hou, *J. Mater. Chem. A* **2022**, *11*, 983.
[17] F. Santos, D. Ivanou, A. Mendes, *Sol. RRL* **2024**, *8*, 2300574.
[18] D. Devadiga, M. Selvakumar, P. Shetty, M. S. Santosh, *J. Electron. Mater.* **2021**, *50*, 3187.
[19] G. Gianola, R. Speranza, F. Bella, A. Lamberti, *Sol. Energy* **2023**, *265*, 112116.
[20] M. Jilakian, T. H. Ghaddar, *ACS Appl. Energy Mater.* **2022**, *5*, 257.
[21] D. Müller, E. Jiang, P. Rivas-Lazaro, C. Baretzky, G. Loukeris, S. Bogati, S. Paetel, S. J. C. Irvine, O. Oklobia, S. Jones, D. Lamb, A. Richter, G. Siefer, D. Lackner, H. Helmers, C. Teixeira, D. Forgács, M. Freitag, D. Bradford, Z. Shen, B. Zimmermann, U. Würfel, *ACS Appl. Energy Mater.* **2023**, *6*, 10404.
[22] J. B. Patel, P. Tiwana, N. Seidler, G. E. Morse, O. R. Lozman, M. B. Johnston, L. M. Herz, *ACS Appl. Mater. Interfaces* **2019**, *11*, 21543.
[23] S. W. Lee, S. Kim, S. Bae, K. Cho, T. Chung, L. E. Mundt, S. Lee, S. Park, H. Park, M. C. Schubert, S. W. Glunz, Y. Ko, Y. Jun, Y. Kang, H. S. Lee, D. Kim, *Sci. Rep.* **2016**, *6*, 38150.
[24] P. Mani, S. V. Nair, M. Shanmugam, *Emerg. Mater.* **2020**, *3*, 117.
[25] A. Roy, S. Sundaram, T. K. Mallick, *ChemistrySelect* **2021**, *6*, 1541.
[26] H. Chen, Y. H. Wu, H. Ma, J. Bin Shi, X. W. Pan, B. X. Lei, Z. F. Sun, *Thin Solid Films* **2020**, *709*, 138205.
[27] M. Shakeel Ahmad, A. K. Pandey, N. Abd Rahim, *Renewable Sustainable Energy Rev.* **2017**, *77*, 89.
[28] J. M. Abisharani, S. Balamurugan, A. Thomas, S. Devikala, M. Arthanareeswari, S. Ganesan, M. Prakash, *Sol. Energy* **2021**, *218*, 552.

[29] M. Stojanović, N. Flores-Diaz, Y. Ren, N. Vlachopoulos, L. Pfeifer, Z. Shen, Y. Liu, S. M. Zakeeruddin, J. V. Milić, A. Hagfeldt, *Helv. Chim. Acta* **2021**, *104*, 2000230.
[30] D. Devadiga, M. Selvakumar, P. Shetty, M. S. Santosh, *J. Power Sources* **2021**, *493*, 229698.
[31] M. Li, F. Igbari, Z. K. Wang, L. S. Liao, *Adv. Energy Mater.* **2020**, *10*, 2000641.
[32] H. Rahmani, D. Shetty, M. Wagih, Y. Ghasempour, V. Palazzi, N. B. Carvalho, R. Correia, A. Costanzo, D. Vital, F. Alimenti, J. Kettle, D. Masotti, P. Mezzanotte, L. Roselli, J. Grosinger, *IEEE J. Microwaves* **2023**, *3*, 237.
[33] F. Bella, C. Gerbaldi, C. Barolo, M. Grätzel, *Chem. Soc. Rev.* **2015**, *44*, 3431.
[34] F. Bella, S. Galliano, M. Falco, G. Viscardi, C. Barolo, M. Grätzel, C. Gerbaldi, *Green Chem.* **2017**, *19*, 1043.
[35] C. T. Li, R. Y. Y. Lin, J. T. Lin, *Chem. Asian J.* **2017**, *12*, 486.
[36] D. Sayah, T. H. Ghaddar, *ACS Sustainable Chem. Eng.* **2024**, *12*, 6424.
[37] S. Galliano, F. Bella, C. Gerbaldi, M. Falco, G. Viscardi, M. Grätzel, C. Barolo, *Energy Technol.* **2017**, *5*, 300.
[38] J. H. Kim, D. H. Kim, J. H. So, H. J. Koo, *Energies* **2022**, *15*, 219.
[39] M. S. Su'ait, M. Y. A. Rahman, A. Ahmad, *Sol. Energy* **2015**, *115*, 452.
[40] W. Yang, W. Yang, J. Zeng, Y. Chen, Y. Huang, J. Liu, J. Gan, T. Li, H. Zhang, L. Zhong, X. Peng, *Prog. Mater. Sci.* **2024**, *144*, 101264.
[41] M. Rayung, M. M. Aung, S. C. Azhar, L. C. Abdullah, M. S. Su'ait, A. Ahmad, S. N. A. M. Jamil, *Materials* **2020**, *13*, 838.
[42] M. M. Hasan, M. D. Islam, T. U. Rashid, *Energy Fuels* **2020**, *34*, 15634.
[43] J. C. De Haro, E. Tatsi, L. Fagiolari, M. Bonomo, C. Barolo, S. Turri, F. Bella, G. Griffini, *ACS Sustainable Chem. Eng.* **2021**, *9*, 8550.
[44] A. Chiappone, F. Bella, J. R. Nair, G. Meligrana, R. Bongiovanni, C. Gerbaldi, *ChemElectroChem* **2014**, *1*, 1241.
[45] A. Johnson Mary Leeda Rani, A. Gunasekeran, D. Sundaramurthy, A. Sambandam, *New J. Chem.* **2022**, *46*, 13156.
[46] A. Gunasekaran, A. Sorrentino, A. M. Asiri, S. Anandan, *Sol. Energy* **2020**, *208*, 160.
[47] S. Galliano, F. Bella, M. Bonomo, G. Viscardi, C. Gerbaldi, G. Boschloo, C. Barolo, *Nanomaterials* **2020**, *10*, 1.
[48] A. Scalia, F. Bella, A. Lamberti, S. Bianco, C. Gerbaldi, E. Tresso, C. F. Pirri, *J. Power Sources* **2017**, *359*, 311.
[49] Q. Zeng, Y. Lai, L. Jiang, F. Liu, X. Hao, L. Wang, M. A. Green, *Adv. Energy Mater.* **2020**, *10*, 1903930.
[50] R. Speranza, P. Zaccagnini, A. Scalia, E. Tresso, A. Lamberti, *J. Power Sources* **2023**, *583*, 233581.
[51] R. Speranza, M. Reina, P. Zaccagnini, A. Pedico, A. Lamberti, *Electrochim. Acta* **2023**, *460*, 142614.
[52] R. Speranza, P. Zaccagnini, A. Sacco, A. Lamberti, *Sol. RRL* **2022**, *6*, 2200245.
[53] C. Law, O. Moudam, S. Villarroya-Lidon, B. O'Regan, *J. Mater. Chem.* **2012**, *22*, 23387.
[54] N. Masud, H. K. Kim, *ACS Omega* **2023**, *8*, 6139.
[55] S. K. Thomas, A. Pockett, K. Seunarine, M. Spence, D. Raptis, S. Meroni, T. Watson, M. Jones, M. J. Carnie, *Inter. Things* **2022**, *3*, 109.
[56] J. Xu, S. H. Reddy, L. A. Castriotta, S. K. Podapangi, M. Luce, A. Cricenti, A. Di Carlo, T. M. Brown, *Sustainable Energy Fuels* **2023**, *7*, 3404.
[57] A. Hagfeldt, G. Boschloo, L. Sun, L. Kloo, H. Pettersson, *Chem. Rev.* **2010**, *110*, 6595.
[58] M. Aftabuzzaman, S. Sarker, C. Lu, H. K. Kim, *J. Mater. Chem. A* **2021**, *9*, 24830.
[59] K. Zhu, S. R. Jang, A. J. Frank, *J. Phys. Chem. Lett.* **2011**, *2*, 1070.
[60] P. Nagaraj, A. Sasidharan, V. David, A. Sambandam, *Polymers* **2017**, *9*, 667.
[61] K. Nonomura, N. Vlachopoulos, E. Unger, L. Häggman, A. Hagfeldt, G. Boschloo, *J. Electrochem. Soc.* **2019**, *166*, B3203.
[62] P. Zaccagnini, L. H. Heß, L. Baudino, M. Laurenti, M. Serrapede, A. Lamberti, A. Balducci, *Adv Mater Interfaces* **2023**, *10*, 2202470.
[63] J. Kim, H. Van Hoai, G. J. Bahk, K. Kwak, K. K. Lee, *Carbon Lett.* **2021**, *31*, 973.
[64] Y. Tang, L. Lu, X. Zang, B. Wang, X. Ye, *ChemSusChem* **2023**, *16*, e202300357.
[65] S. Dsoke, X. Tian, C. Täubert, S. Schlüter, M. Wohlfahrt-Mehrens, *J. Power Sources* **2013**, *238*, 422.
[66] A. Railanmaa, S. Lehtimäki, D. Lupo, *Appl. Phys. A: Mater. Sci. Process* **2017**, *123*, 1.
[67] A. Willfahrt, E. Steiner, J. Hötzel, X. Crispin, *Appl. Phys. A: Mater. Sci. Process* **2019**, *125*, 474.
[68] X. Yue, J. Kiely, D. Gibson, E. M. Drakakis, *IEEE Trans. Ind. Electron.* **2020**, *67*, 2411.
[69] H. Wada, K. Yoshikawa, S. Nohara, N. Furukawa, H. Inoue, N. Sugoh, H. Iwasaki, C. Iwakura, *J. Power Sources* **2006**, *159*, 1464.
[70] M. Matsui, M. Kotani, Y. Kubota, K. Funabiki, J. Jin, T. Yoshida, S. Higashijima, H. Miura, *Dyes Pigm.* **2011**, *91*, 145.
[71] V. Vega-Garita, L. Ramirez-Elizondo, N. Narayan, P. Bauer, *Prog. Photovolt: Res. Appl.* **2019**, *27*, 346.
[72] A. Scalia, A. Varzi, A. Lamberti, T. Jacob, S. Passerini, *Front. Chem.* **2018**, *6*, 443.
[73] M. Aftabuzzaman, Masud, H. Zhou, H. M. Kim, Y. Kang, H. K. Kim, *Small* **2024**, *20*, 2302826.
[74] Y. Lu, M. Chen, G. Zhu, Y. Zhang, *Nanoscale* **2024**, *16*, 8778.
[75] R. Zhou, B. Guo, W. Wu, H. Wang, H. Niu, L. Wan, *IEEE Trans. Electron Devices* **2024**, *71*, 7609.
[76] V. Sharma, R. Kumar, N. Arora, S. Singh, N. Sharma, A. Anand, S. K. Jain, S. Sharma, *J. Solid State Electrochem.* **2020**, *24*, 1337.